ARTICLE   OPEN

Check for updates

Controlling sulfurization of 2D Mo$_2$C crystal for Mo$_2$C/MoS$_2$-based memristor and artificial synapse

Xin Tang[1], Leilei Yang[1,2], Junhua Huang[1], Wenjun Chen[3], Baohua Li[1], Shaodian Yang[1], Rongliang Yang[1], Zhiping Zeng[4], Zikang Tang[5] and Xuchun Gui[1]✉

Owing to the conductance-adjustable performance, the emerging two-terminal memristors are promising candidates for artificial synapses and brain-spired neuromorphic computing. Although memristors based on molybdenum disulfide (MoS$_2$) have displayed outstanding performance, such as thermal stability and high energy efficiency, reports on memristors based on MoS$_2$ as the functional layer to simulate synaptic behavior are limited. Herein, a homologous Mo$_2$C/MoS$_2$-based memristor is prepared by partially sulfuring two-dimensional Mo$_2$C crystal. The memristor shows good stability, excellent retention ($\sim 10^4$ s) and endurance (>100 cycles), and a high ON/OFF ratio (>10^3). Moreover, for comprehensively mimicking biological synapses, the essential synaptic functions of the device are systematically analyzed, including paired-pulse facilitation (PPF), short-term plasticity (STP), long-term plasticity (LTP), long-term depression (LTD), and the transitions from STP to LTP. Notably, this artificial synapse could keep a high-level stable memory for a long time (60 s) after repeated stimulation. These results prove that our device is highly desirable for biological synapses, which show great potential for application in future high-density storage and neuromorphic computing systems.

INTRODUCTION

Inspired by highly connected and extremely energy-efficient biological neural system, researchers have put forward a computing system consisting of artificial neurons[1,2], which can not only solve the bottleneck effectively that computers based on Von-Neumann architecture are facing, but lead to a generation of powerful computing paradigms[3,4]. Among various devices used for mimicking synapses, including memristors[5,6], complementary metal-oxide-semiconductor transistors[7,8] and phase change memories[9], memristors have been considered as one of the most promising electronic devices for neuromorphic computing owing to their intrinsic capability to remember historical states[10–13]. As a representative of transition metal dichalcogenides (TMDCs), MoS$_2$ is widely applied in various devices such as memristors[14,15], field-effect transistors[16,17], and photodetectors[18,19] due to its abundant sulfur vacancies, semiconductor characteristics and tunable bandgap. Currently, MoS$_2$-based memristors have reached some performance milestones and achieved some intriguing applications[20–23]. For instance, due to the atomic-scale thickness and electrochemical metallization (ECM), the switching voltage of the MoS$_2$ double-layer memristor can be lowered to 0.1–0.2 V[20]. A fully printed Ag/MoS$_2$/Ag memristor exhibits a high switching ratio of 10^7, a wide range of tunable resistance states of 10–10^{10} Ω, and a switching energy of 4.5 fJ per transition set[21]. With high-quality crystal, an atomically sharp interface, and the assistance of oxygen atoms doping, the MoS$_2$-based memristor shows excellent switching performance with an endurance of up to 10^7 and an operating temperature of 340 °C[22]. In addition, four-terminal lateral memristors with artificial engineered grain boundaries in monolayer MoS$_2$ can not only respond to electric and light stimulation simultaneously, but also imitate biological learning

and cognitive processes as well as image perception and processing[23]. In all, most of the reported MoS$_2$ memristors have outstanding switching performance and tunable window voltages, compared with those using transition metal oxides (TMOs) as functional materials. However, reports on memristors with MoS$_2$ as the functional layer to simulate synaptic behavior are limited, and transition from short-term plasticity (STP) to long-term plasticity (LTP) based on MoS$_2$ synaptic also need further investigation[24–27].

For an electronic device based on two-dimensional (2D) materials, its performance can be greatly improved by reducing the contact resistance and potential barrier between the active layer and the electrodes. There have been various strategies to solve the problem of large contact resistance between semiconductor materials and metal electrodes, such as phase engineering[28], doping[29], inserting a tunneling layer into the interface to form a metal-insulator-semiconductor contact structure[30], and using graphene/soft-landed metals as vdW-interfaced electrodes[31]. Similarly, for memristors, using the above methods to optimize the contact between the memristive layer and the electrodes can also improve their performance. For example, by introducing graphene as contact electrodes, the MoS$_{2-x}$O$_x$-based memristor could switch in more than 100 ns and over 2×10^7 cycles. This high switching performance is primarily benefitted from a high-quality interface between graphene and MoS$_{2-x}$O$_x$[22]. By forming a variable-barrier WSe$_2$/graphene Schottky junction, the WO$_x$-based memristor exhibits gate-tunable memristive switching characteristics with programming voltages of 0.2–0.5 V, and implements fundamental synaptic functions[32]. In addition, the InSe$_2$-based memristor fabricated by van der Waals electrodes integration has an ultralow set/reset voltage of 0.12 /0.04 V, which is attributed to the atomically clean and sharp

[1]State Key Laboratory of Optoelectronic Materials and Technologies, School of Electronics and Information Technology, Sun Yat-sen University, Guangzhou 510275, China. [2]Department of physics, Guangxi Minzu University, Nanning 530006, China. [3]School of Electronic Information Engineering, Foshan University, Foshan 528000, P. R. China. [4]School of Materials Science and Engineering, Sun Yat-sen University, Guangzhou 510275, China. [5]Institute of Applied Physics and Materials Engineering, University of Macau, Avenida da Universidade, Taipa, Macau 999078, China. ✉email: guixch@mail.sysu.edu.cn

interface between electrodes and the channel[33]. Mo$_2$C, as a metallic 2D material with low work function (3.8 eV), can improve the contact with semiconductor materials[34–36]. It has been reported that an excellent contact resistance as low as 2.1 kΩ·μm could be formed between Mo$_2$C and MoS$_2$[34]. Moreover, by inserting Mo$_2$C between the metal electrodes and 2D MoO$_x$, the contact barrier is lowered and the performance of two-terminal MoO$_x$-based device is enhanced[37]. Hence, it is appealing and significant to design a Mo$_2$C/MoS$_2$-based memristor and study its application in mimicking synapses by inserting Mo$_2$C into the contact interface.

Here, a strategy for fabricating vertical two-terminal memristor based on Mo$_2$C/MoS$_2$ heterostructure is proposed, by which Mo$_2$C is partially sulfurized to obtain a seamless interface. The device based on this homologous heterostructure exhibits stable memristive performance with retention time up to 10^4 s, endurance up to 100 cycles, and on/off ratio up to 10^3. Meanwhile, it can be used to simulate biological synaptic functions, including paired-pulse facilitation (PPF), STP, LTP, and long-term depression (LTD). Furthermore, the regulation of PPF and the transitions from STP to LTP by applying continuous pulses have been discussed systematically. It is found that the artificial synapse can maintain a high level of memory after the end of the stimulation for a long time, that is, the memristor can maintain stable long-term memory. Therefore, the proposed device is a promising candidate for high-density storage and neuromorphic computing applications.

RESULTS

Fabrication and characterization of the Mo$_2$C/MoS$_2$ heterostructure

The Mo$_2$C/MoS$_2$ heterostructure is prepared by controlling sulfurization of 2D Mo$_2$C crystal, which is synthesized by CVD, as reported in our early work[36]. After sulfurization, several layers on the top surface of Mo$_2$C could convert to MoS$_2$, and form an integrated Mo$_2$C/MoS$_2$ heterostructure, as illustrated in Fig. 1a. After deposition of the top electrode (Ni/Au) at the surface of MoS$_2$ and the bottom electrode (Ni/Au) on the p^{++} Si substrate (Fig. 1b), the heterostructure can be directly used as a memristor. Detailed fabricating process of materials and devices is described in Methods. The optical microscope (OM) image displays that the

as-grown 2D Mo$_2$C crystal is mainly in a regular hexagon with the size of ~15 μm (Fig. 1c). More morphology and structural characteristics of the Mo$_2$C are shown in Supplementary Fig. 1. Atomic force microscopy (AFM) results show that the thickness and surface roughness of the Mo$_2$C is about 84 nm and 1.05 nm, respectively, indicating the excellent flatness of multilayer 2D Mo$_2$C (Fig. 1d).

The Mo$_2$C/MoS$_2$ heterostructure becomes darker after sulfurization, while it maintains the same hexagonal shape as the pristine Mo$_2$C (Fig. 1e). It suggests that the sulfurization process did not destroy the morphology and structure of the sample. The degree of sulfurization of the sample can be controlled by changing the sulfurization temperature and time during CVD process, similar to the oxidation of Mo$_2$C crystal[36]. Figure 1f shows the Raman spectra of the Mo$_2$C/MoS$_2$. Compared with the Raman spectra of the Mo$_2$C (Supplementary Fig. 1), additional characteristic peaks at 182.1, 380.3, 410.5, 457.6, and 635.2 cm^{-1} are collected for the Mo$_2$C/MoS$_2$, while the characteristic peak (143.5 cm^{-1}) of B$_{3g}$ mode for Mo$_2$C is significantly weakened. The peak at 380.3 cm^{-1} corresponds to E$^1_{2g}$ mode of MoS$_2$, resulting from the opposite vibration of two S atoms with respect to the Mo atom. The peak at 410.5 cm^{-1} represents A$_{1g}$ mode, which is associated with the out-of-plane vibration of only S atoms in opposite directions[38]. Besides, the peaks at 182.1, 457.6, and 635.2 cm^{-1} are resulted from the resonance Raman (RR) scattering[38]. These results indicate that the surface layers of Mo$_2$C have been successfully converted to MoS$_2$. Moreover, the Raman mapping images of the Mo$_2$C/MoS$_2$ heterostructure at its characteristic peak show a uniform intensity distribution, indicating the homogeneity of the as-synthesized MoS$_2$ on Mo$_2$C (Fig. 1g and Supplementary Fig. 2). X-ray photoelectron spectroscopy (XPS) results further confirm the formation of the Mo$_2$C/MoS$_2$ heterostructure, as shown in Fig. 1h. The high-resolution Mo 3d XPS of the Mo$_2$C/MoS$_2$ heterostructure presents the doublet peaks of Mo^{2+} (228.6 and 231.8 eV), and Mo^{4+} (229.5 and 232.7 eV), which mean the coexistence of Mo$_2$C and MoS$_2$, respectively[36,39]. The weak signal of MoO$_3$ (doublet peaks of Mo^{6+} at 233.1 and 236.7 eV) is due to the bonding of Mo atoms with O atoms in the air. The XPS survey spectra and high-resolution of C1s are shown in Supplementary Fig. 3. Thus, a uniform Mo$_2$C/MoS$_2$ heterostructure has been fabricated by the sulfurization of the 2D Mo$_2$C crystal. To further demonstrate the
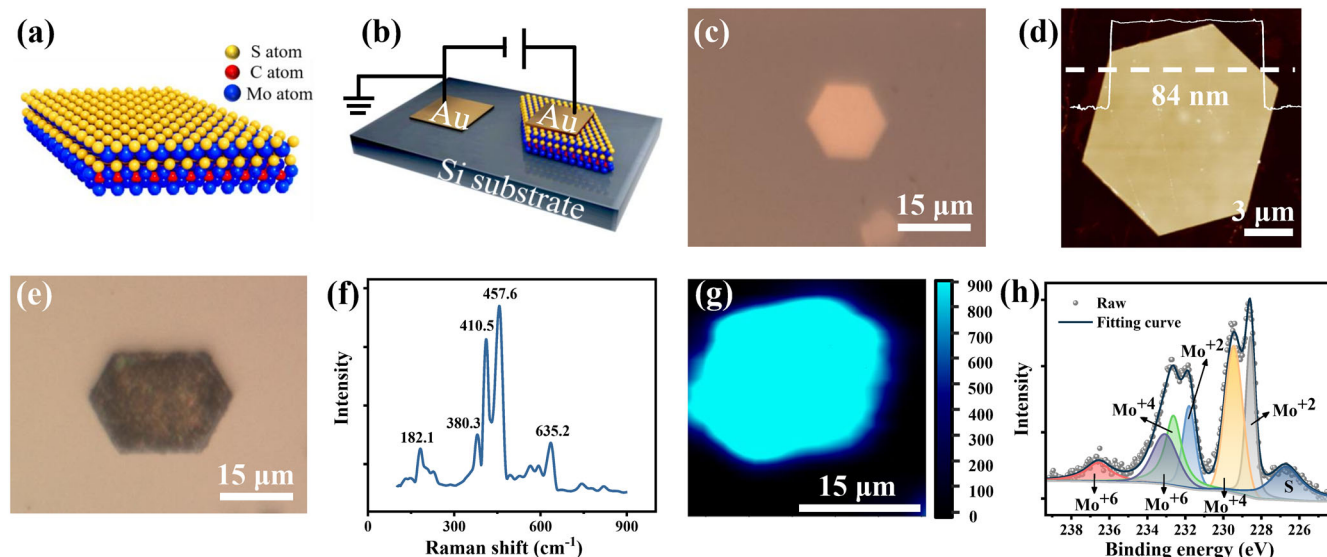
Fig. 1 Structure characteristics of the 2D Mo$_2$C/MoS$_2$ heterostructure. a Schematic illustration of the Mo$_2$C/MoS$_2$ heterostructure. **b** Schematic illustration of the measurement of the electrical properties of the device, where Ni/Au electrodes are deposited on the surface of MoS$_2$ and Si substrate, respectively. **c** OM, and **d** AFM image of the as grown 2D Mo$_2$C crystal. **e** OM, **f** Raman spectra, **g** Raman mapping of the intensity at the peak of 410.5 cm^{-1}, and **h** XPS of the 2D Mo$_2$C/MoS$_2$ heterostructure.
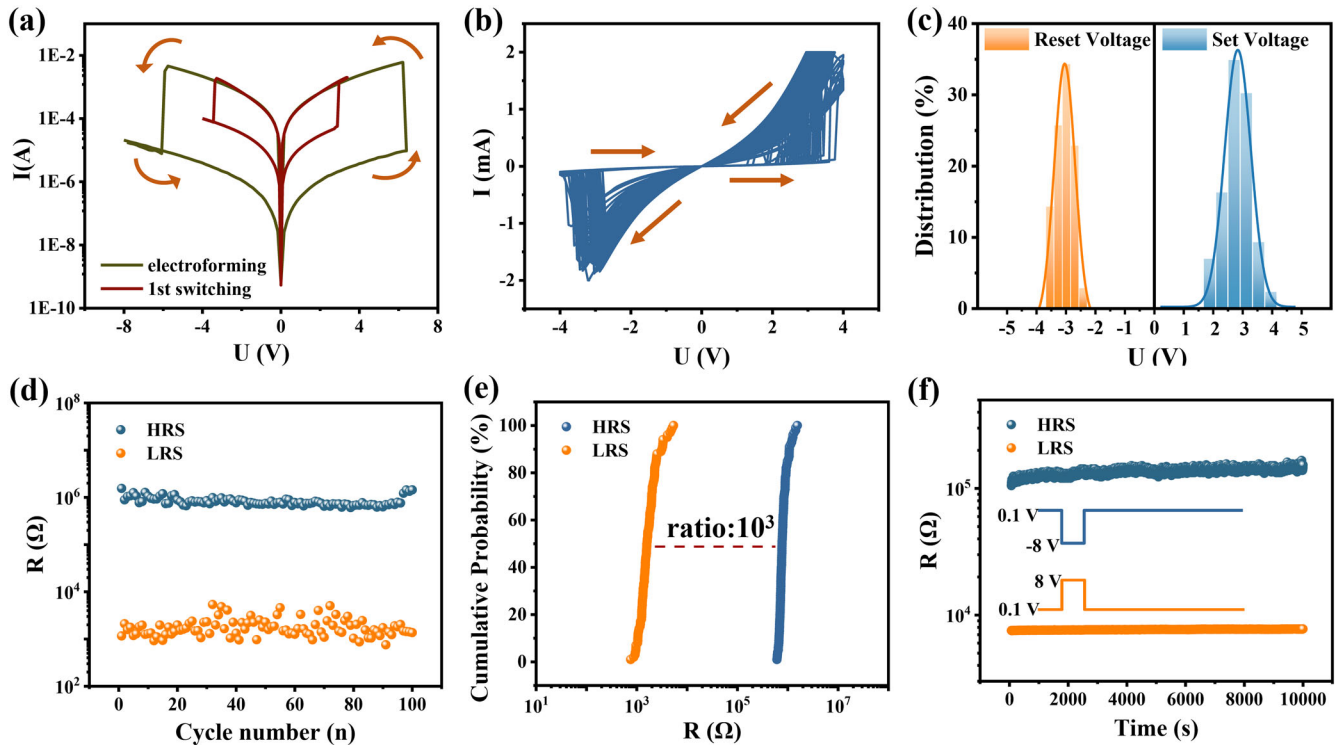
Fig. 2 Electrical characterizations of the memristor. a *I-V* switching curves of the device. The green and red line represents the electroforming and the 1st switching process, respectively. **b** *I-V* curves of the device for 100 consecutive cycles of sweep volatges. **c** The distribution of Set voltage and Reset voltage during 100 cycles. **d** Endurance characteristics undergoing 100 SET/RESET switching cycles. **e** Cumulative probability plots of HRS and LRS. **f** Retention performance of LRS and HRS after Set and Reset operations. The pulse voltages and read voltages are 8/−8 V, and 0.1 V, respectively.

interface characteristics of Mo_2C/MoS_2 heterostructure, the samples are analyzed by high-resolution transmission electron microscope (HRTEM). From the HRTEM images of the cross-sectional of Mo_2C/MoS_2 (Supplementary Fig. 4), it can be seen that there is a very clear boundary between Mo_2C and MoS_2, indicating its seamless structure (Supplementary Fig. 4b). In addition, the Mo_2C crystal maintains original single structure with d-spacing of 3.7 Å, which is in consistent with the (110) plane of Mo_2C (Supplementary Fig. 4c)[40]. In the MoS_2 region, the major d-spacing is 3.1 Å corresponding to the (004) plane (Supplementary Fig. 4d). This further confirms the structural transition of the samples from Mo_2C to MoS_2.

Electrical characterizations of the memristor
To examine the switching performance of the Mo_2C/MoS_2-based memristor, the samples are systematically tested for their electrical properties. Figure 2a shows the typical bipolar current-voltage (*I-V*) curve of the device. During the test, a forward voltage is applied between the top electrode (connected with MoS_2) and the bottom electrode. Initially, the device requires an electroforming process with a larger sweep voltage (−8 to 8 V) to achieve the switching process between the high-resistance state (HRS, i.e., OFF state) and the low-resistance state (LRS, i.e., ON state). Then, the device can operate at lower voltages, such as a smaller sweep voltage (−4 to 4 V) for the 1st switching process (Fig. 2a). The process of ON switching is defined as SET, where the voltage is about 2.9 V. Next, an opposite-polarity bias sweep is applied to bring the device back to the HRS at the voltage of proximately −3 V (defined as RESET). Linear *I-V* curves of electroforming and 1st switching process are displayed in Supplementary Fig. 5. It can be calculated that the power consumption of the device is 0.16 mW. It is essential to verify the reliability and nonvolatility of our device as a memristor, so 100 consecutive cycles of sweep voltage from

−4 to 4 V are employed to the device (Fig. 2b). As a result, the memristor could maintain stable switching behaviors of HRS and LRS in 100 cycles. At a higher sweep voltage of −8 to 8 V, the device also exhibits high stability (Supplementary Fig. 5c), which indicates that the memristor has a wide operating voltage. Figure 2c displays the distribution of SET and RESET voltage of 100 cycles, the corresponding standard deviation (σ) of which are 0.45 and 0.35 V, respectively. Additionally, it is found that the memristor possesses threshold voltages with a mean value of 2.83 and −3.04 V, which are larger than other reported vertical memristors[12,41–43]. Such large threshold voltages are attributed to large activation energy and migration of sulfur ions in MoS_2[44–46]. The device at a sweep voltage from −8 to 8 V shows a resistance of 10^6 and 10^3 Ω at HRS and LRS, respectively. The resistance for both states maintains steady during the sweep cycles (Fig. 2d). The cumulative probability of the HRS and LRS resistance is further calculated and shown in Fig. 2e. It exhibits HRS/LRS ratio of ≈10^3 in all cycles, indicating the reproducibility of such a memristor during cycle-to-cycle measurement. Supplementary Fig. 6 displays the distribution and cumulative probability of HRS and LRS at a sweep voltage from −4 to 4 V. Figure 2f illustrates the retention characterization of LRS and HRS after applying the corresponding pulse (amplitude:8 V for SET and −8 V for RESET, read voltage: 0.1 V), which shows no noticeable change during the test time (>10^4 s), indicating the reliable nonvolatility of the memristor. It is worth noting that the HRS/LRS ratio for endurance statistics is bigger than that for retention statistic due to the difference of the read voltage.

To analyze the underlying conduction mechanism of the memristor, we have plotted and fitted the *I-V* curves by $I \propto V^{\alpha}$ corresponding to HRS and LRS of the electroforming process (Fig. 3a and b), respectively. The results show that the *I-V* curve can be divided into three regions according to the value of α,
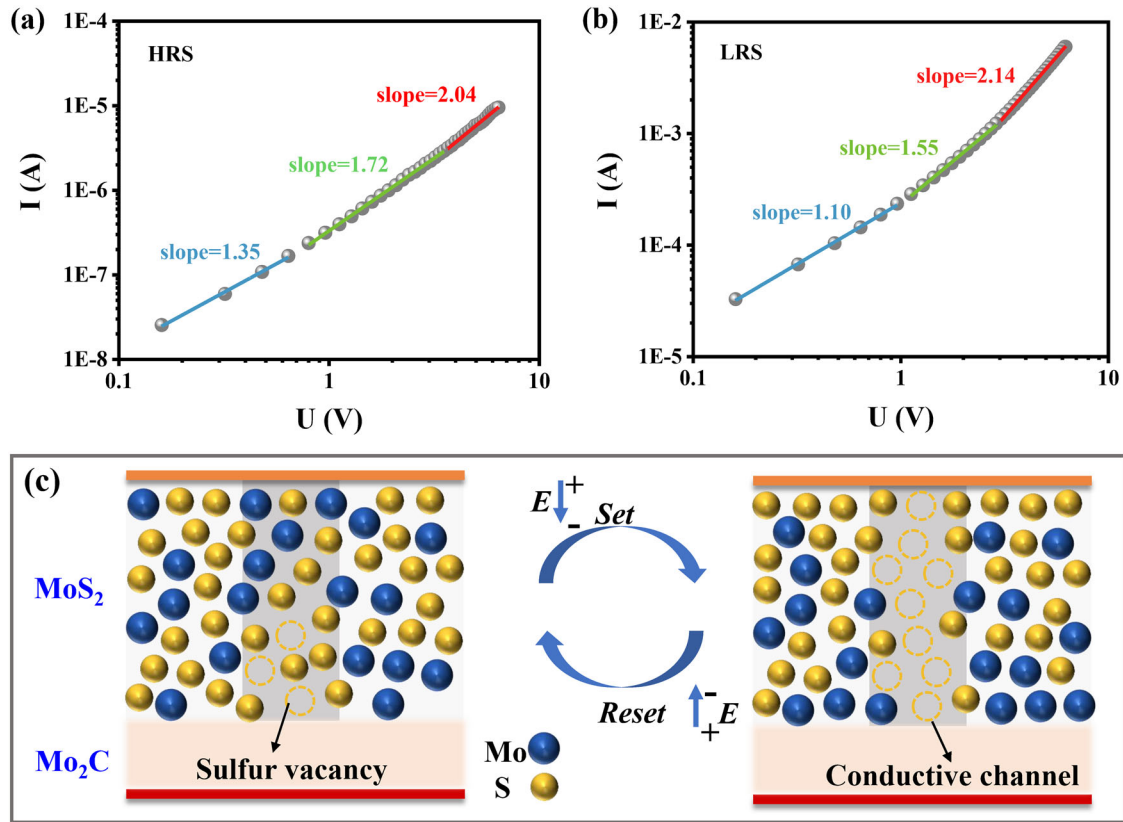
Fig. 3 Conductive and memristive mechanism of the Mo₂C/MoS₂ heterostructure. I-V curves of (**a**) HRS and (**b**) LRS in the electroforming process. **c** Schematic illustration of the memristive mechanism of transformation back and forth from HRS to LRS under electric fields.

which represents the slope of the curve. The conduction mechanism of the sample in this work conforms to the space charge limited conduction (SCLC)[47–49]. At low voltage, it exhibits ohmic conductive behaviors, implying that the concentration of thermally generated free carriers is larger than that of the injected carriers. With the increasing voltage, the current gradually increases, and the slope (a) is >2 as the voltage is larger than 4 V. It indicates that the injected charge density exceeds the intrinsic free carrier density and Child's law becomes the main conductive mechanism. Afterwards, the device is reset to LRS and the fitting result is similar to that of HRS. Note that the conductive filament is usually formed by activating metal ions, such as Cu and Ag, driven by external bias in ECM mechanism-based memristors[20,50]. In contrast, the memristor in this work is based on inert electrodes -Ni/Au, which cannot be ionized under electric field and is not easy to adsorb oxygen atoms. Thus, we claim that our memristor is likely to be a valance change memory (VCM) device[12,22,51], in which sulfur vacancies move to form conductive channels. Figure 3c illustrates the distribution of sulfur vacancies during HRS and LRS. When a forward electric field is applied to the device, a large number of sulfur vacancies appear in MoS₂ layers due to the migration of sulfur ions. Therefore, the conductive channels are formed, leading to the conversion from HRS to LRS. For the rupture of conductive channels that reset the device back to the HRS, it is ascribed to the reverse diffusion of sulfur ions to fill sulfur vacancies under a reverse electric field. A similar mechanism of MoS₂-based memristor is also confirmed by in situ characteristics of sulfur vacancies, which are reported by other previous works[42,52,53].

Artificial synaptic characteristics of the memristor

The memristor based on the Mo₂C/MoS₂ heterostructure can also be used for simulating synaptic behaviors. As five continuous

positive and negative sweep voltages are applied to the device, the conductance increases (decreases) with positive (negative) sweep voltages (Fig. 4a). It means gradual changes of the conductance under continuous voltage stimulations, which is analogous to the behavior of biosynapse, reflecting a successively variable of synaptic weight[54]. Usually, as two consecutive pulses are successively applied to a memristor, the phenomenon in which the second pulse generates a larger postsynaptic current (PSC) than the first one is called PPF[55]. Obviously, the memristor in this work exhibits an obvious PPF characteristic when they are applied two continuous pulses, as shown in Fig. 4b. Note that PPF index is expressed by:

$$PPF = \frac{I_2 - I_1}{I_1} \times 100\% \qquad (1)$$

Where I_1 and I_2 are the PSC corresponding to the first and second pulse, respectively. Accordingly, PPF index in Fig. 4b is about 47.4%. In addition, the enhancement of the PSC is related to the parameter of pulses, including the interval, width and amplitude. In Fig. 4c, a pair of positive pulses with interval varying from 20 to 1000 ms is applied to another device. It is found that the value of the PPF index gradually decreases with the increasing time interval, which is in agreement with the behavior of biological synapses. Furthermore, the PPF index can be fitted by a double-phase exponential function (pink line in Fig. 4c):

$$PPF = C_1 \times exp\left(-\frac{t}{\tau_1}\right) + C_2 \times exp\left(-\frac{t}{\tau_2}\right) \qquad (2)$$

where t is the pulse interval time, C_1 and C_2 are the initial facilitation magnitudes, τ_1 and τ_2 are the characteristic relaxation time[55]. The results show that τ_1 and τ_2, are about 145.4 and 932.0 ms, corresponding to the fast and slow facilitation terms, respectively. Figure 4d exhibits the post-tetanic potentiation (PTP)
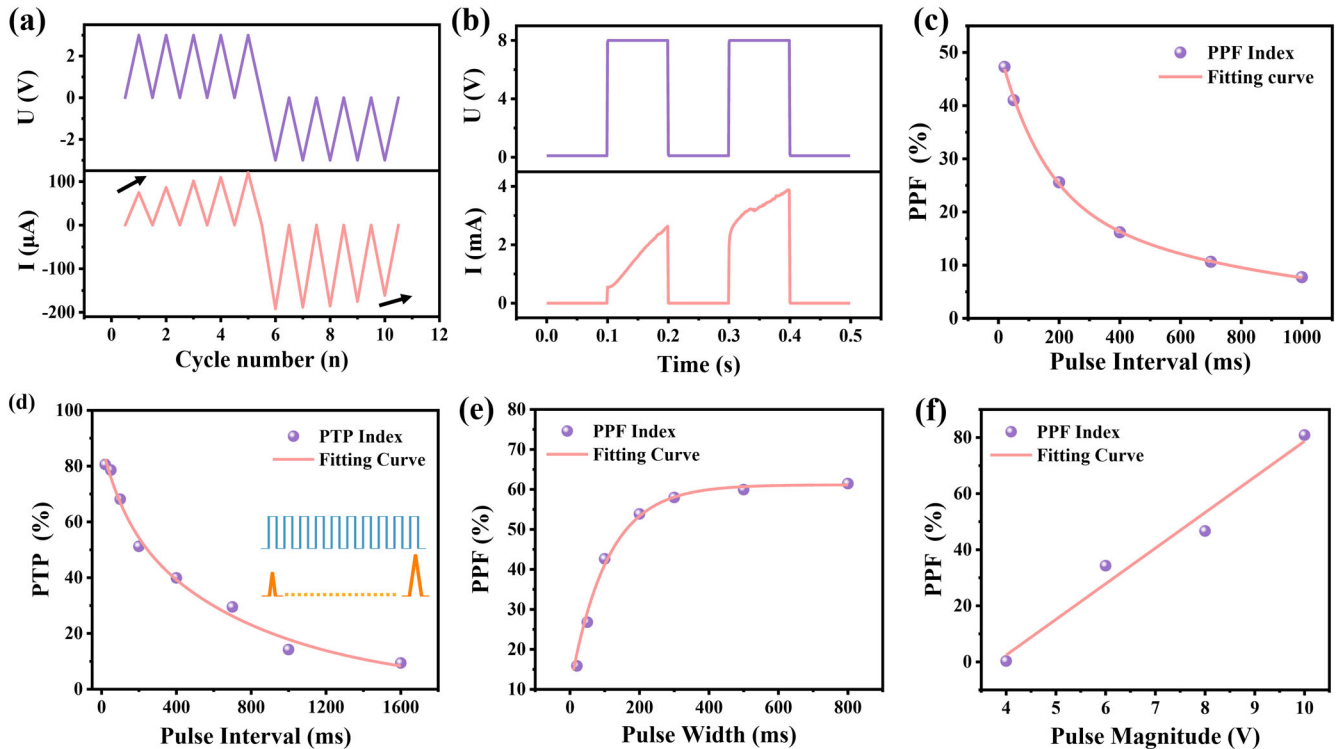
Fig. 4 Artificial synaptic characteristics of the memristor. a Variations of voltage and current with respect to sweep cycles. **b** Emulations of PPF behaviors. The test parameters are pulse amplitude of 8 V, width of 100 ms, interval of 100 ms, and read voltage of 0.1 V. **c** The PPF indexes at different pulse interval, which varies from 20 to 1000 ms. **d** The PTP indexes versus pulse interval, which varies from 20 to 1600 ms. The PPF indexes versus pulse (**e**) width, and (**f**) magnitude, which varies from 10 to 800 ms, and from 4 to 10 V, respectively.

index versus the interval time with ten consecutive pulses applied to the device. Here, the PTP index is defined as:

$$PTP = \frac{I_{10} - I_1}{I_1} \times 100\% \qquad (3)$$

Where I_1 and I_{10} are the PSC corresponding to the first and tenth pulse, respectively. Similar to the PPF, the index of PTP also decreases with increasing pulse intervals. However, the PTP index is larger than the PPF index. As applying pulses with different widths and amplitudes on the device, it also exhibits behavior similar to biosynapse (Fig. 4e, f). As the pulse width increases, the PPF index first increases and then reaches saturation. And the increasing amplitude triggers the linear increase of PPF index. The increasing trend in both cases is due to the presence of more sulfur vacancies in the material.

In order to show the characteristic of PSC, pulses trains of the device with different amplitudes, widths and intervals are performed (Supplementary Fig. 7). When the amplitude of pulses increases from 6 V to 10 V, the initial current is larger and PSC increases more significantly. In addition, the regulation of current by pulse width shows the same trend as that of pulse amplitude. However, a larger pulse interval leads to a smaller final current. In short, PSC could be well regulated by different amplitude, width, and interval of pulse trains, which facilitates obtaining ideal PSC under suitable pulse stimulation, thus broadening the application of memristors in synapses.

The ability to modulate and retain the synaptic weight over time is defined as synaptic plasticity, namely synaptic potentiation, which represents the level of learning and memory and is divided into STP and LTP[56–58]. Note that short-term depression (STD) and LTD are depression of synaptic weight[59]. To simulate the LTP and LTD of the proposed device, 20 positive and 20 negative pulses are applied in sequential. The PSC response indicates that the artificial synapses can be bidirectionally regulated by a sequence

of positive or negative pulses, which is suitable for application in more complex deep neural networks (Fig. 5a and Supplementary Fig. 8). From previous results about PPF simulations, synaptic plasticity can also be modulated by pulse interval. As shown in Fig. 5b, it could exhibit either STP or LTP using pulses with different intervals ($\Delta t = 100$ ms or 500 ms).

Compared with STP representing short-term memory, LTP is a permanent memory formed by repeated training based on short-term memory, corresponding to the lasting change of synaptic weight. Therefore, two pulse trains with the same interval (100 ms) and different widths (50 ms and 200 ms) are sequentially applied to the device. The result illustrates that pulse trains with wider widths lead to larger PSC after the stimulation, that is, the device can be switched from STP to LTP (Fig. 5c). Through sufficient repeated training, the transition from STP to LTP can also be achieved, resembling the biological synapse. To obtain this transition, we attach pulses with different numbers (5, 10, 20, 40, and 80) to the device and then use a voltage of 1 V to read current within 60 s. As shown in Fig. 5d, the normalized synaptic weight decreases rapidly at the beginning, then decreases slowly, and finally reaches a relatively stable level, indicating a similar trend with the human-memory "forgetting (or retention) curve" in psychology. The decay process and the final synaptic weight can be regarded as STP and LTP, respectively. With the increase of pulse number, the synaptic weight for LTP can be increased from 35% to 77%, suggesting the transition from short- to long-term memory. The experimental decay can be fitted by a double exponential decay function as follows

$$y = y_0 + C_3 \times exp\left(-\frac{t}{\tau_3}\right) + C_4 \times exp\left(-\frac{t}{\tau_4}\right) \qquad (4)$$

where y_0 is the current offset, C_3 and C_4 are the fit constants, τ_3 and τ_4 are the time constants[54]. The fitting result is shown in Fig. 5e, where τ_3 and τ_4 are significantly different from τ_1 and τ_2 in
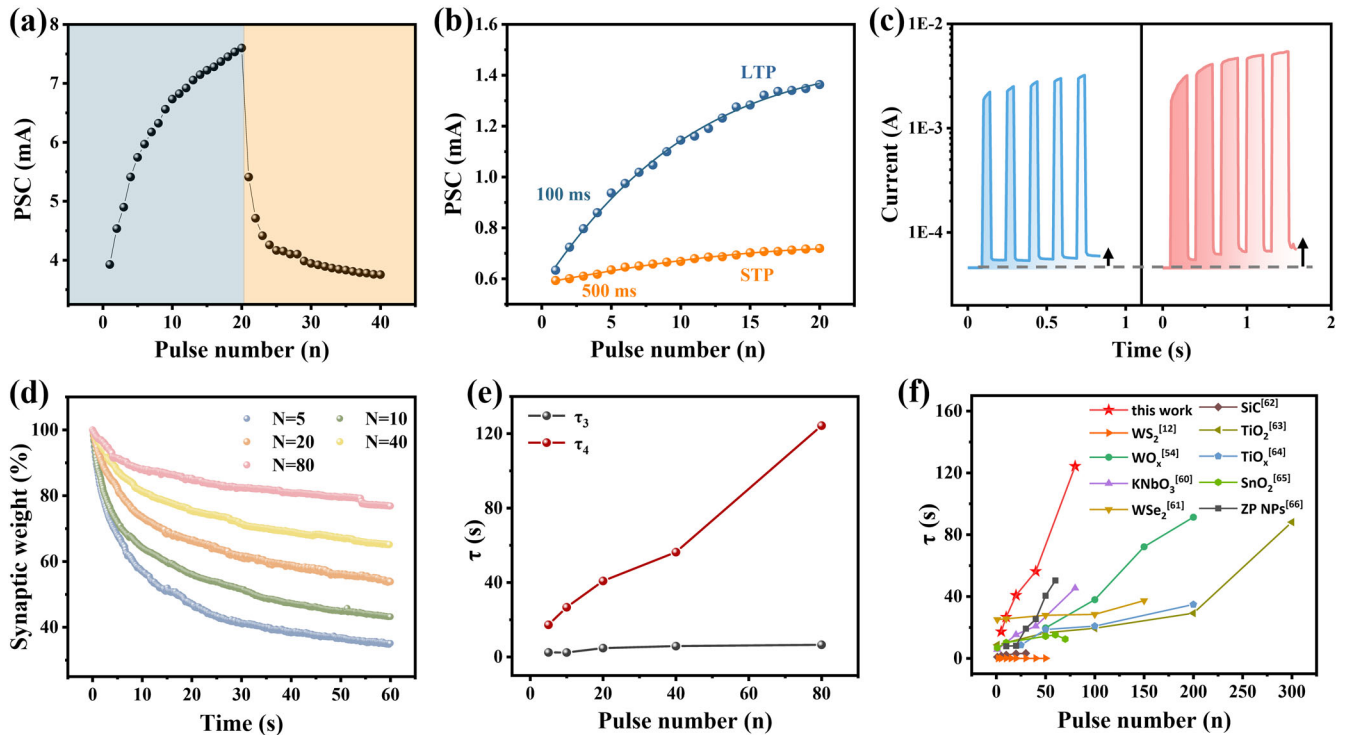
Fig. 5 Artificial synaptic characteristics of the memristor, including STP, LTP, LTD, and transitions from STP to LTP. a PSC values with the increasing of pulse number (pulse amplitude of 8/−8 V, width of 100 ms, interval of 100 ms, and read voltage of 0.1 V), mimicking potentiation/depression behaviors of a biological synapse. **b** PSC values versus the pulse number at pulse interval of 100 ms and 500 ms. **c** Pulse curves for the device after application of a sequence of presynaptic pulses with different width (100 and 300 ms), and same pulse interval of 100 ms. **d** Retention curves for synaptic weight after different numbers of identical presynaptic pulses (pulse amplitude of 8 V, width of 1000 ms, interval of 1000 ms and read voltage of 1 V). **e** The distribution of time constants obtained by fitting. **f** Comparison of time constants for different memristors.

Eq. (2) related to PPF. The decay of the former undergoes repeated pulse stimulation, resulting in more sulfur vacancies accumulating and longer duration time, representing LTP. However, the latter only undergoes two pulses stimulation and the concentration difference of sulfur vacancies is smaller, representing STP. The distribution of τ_3 and τ_4 obtained by fitting are shown in Fig. 5e. τ_3 and τ_4 increase from 2.38 to 6.53 s and from 17.25 to 124.31 s, respectively, indicating a decreasing forgetting rate which further verifies the slower relaxation of synaptic weight by applying more pulses. Figure 5f compares the time constant τ_4 representing the degree of forgetting in this paper with the time constants in other reports. The results show that our device has a very low level of forgetting under the same pulse stimulation, implying a clear advantage in learning ability[12,54,60–66].

DISCUSSION

In summary, a two-terminal memristor based on Mo_2C/MoS_2 heterostructure was fabricated. The device exhibits excellent stability, retention, endurance, and a high HRS/LRS ratio, which is attributed to the good contact brought by introducing Mo_2C. In addition, we indirectly proved that the memristive mechanism is the formation and destruction of conductive channels associated with sulfur vacancies under the electric field. Moreover, the memristor successfully mimicked main biological synaptic functions, including PPF, STP, LTP, LTD, and STP to LTP transitions. The device can not only possess a lower forgetting rate, but also maintain a stable long-term memory under repeated stimulation. Therefore, it can be concluded that our memristor is an excellent candidate for an artificial synapse, which shows great potential in high-density storage and neuromorphic computing applications.

METHODS

Growth and transfer of Mo₂C

The 2D Mo_2C was synthesized by CVD, as reported by our previous work[36]. First, a piece of Cu foil (120 μm in thickness) as the growth substrate was placed on top of a Mo foil (thickness of 50 μm). Then they were put in the middle of the quartz reactor. Before the growth, Cu/Mo foil was heated to 1100 °C in 50 min under a mixture of Ar (200 sccm) and H_2 (100 sccm), then annealed for 25 min. Subsequently, the 2D Mo_2C was grown for 60 min by introducing CH_4 (3 sccm). After growth, the Mo_2C was transferred onto a p^{++} Si substrate with low resistance by the polydimethylsiloxane (PDMS) assisted transfer method.

Preparation of the Mo₂C/MoS₂ hybrid structure

The Mo_2C/MoS_2 hybrid structure was synthesized by sulfurization of 2D Mo_2C. First, the obtained Mo_2C on Si substrate was put in the middle of the quartz reactor, while sulfur powders (Alfa Aesar, precipitated, 99.5%) in moderation were put in the upstream of the heating zone. Then, the tube furnace was heated from ambient temperature to 350 °C under a mixture of Ar (200 sccm) and H_2 (100sccm) in 60 min. Subsequently, the supply of H_2 was cut off and the flow rate of Ar was set as 60 sccm. The temperature of the reactor was raised from 350 °C to 720 °C in 20 min, and the heating temperature of the sulfur powders was set to 170 °C. After the sulfurization for 60 min, a Mo_2C/MoS_2 heterostructure was obtained on the Si substrate.

Sample characterization and measurement of the device

The morphology, composition, and crystal structure of the Mo_2C and the Mo_2C/MoS_2 hybrid were characterized by SEM (Hitachi S-

4800), AFM (Bruker Dimension), OM (HORIBA JY HR800), and XPS (Thermo-VG Scientific, ESCALAB 250Xi). Raman spectra and mapping were collected using HORIBA JY HR800 with a 633 nm exciting laser. TEM images were obtained by Tecnai, G2 F30. With massless photolithography, two square windows with area of 64 μm^2 and 3.6×10^5 μm^2 were carved in the middle of the Mo_2C/MoS_2 sample and the surface of the Si substrate, respectively, followed by depositing Ni/Au of 20/65 nm as electrodes. The electrical characteristics, including DC and pulse measurement, were tested using a probe station with KEYSIGHT B2902A.

DATA AVAILABILITY
Additional data related to this paper may be requested from the authors.

REFERENCES
1. Sun, L. et al. An Artificial Reflex Arc That Perceives Afferent Visual and Tactile Information and Controls Efferent Muscular Actions. *Research* **2022**, 9851843 (2022).
2. Gong, J. et al. An artificial visual nerve for mimicking pupil reflex. *Matter* **5**, 1578–1589 (2022).
3. Mead, C. Neuromorphic Electronic Systems. *Proc. IEEE.* **78**, 1629–1636 (1990).
4. Yu, S. Neuro-Inspired Computing With Emerging Nonvolatile Memory. *Proc. IEEE.* **106**, 260–285 (2018).
5. Sun, K., Chen, J. & Yan, X. The Future of Memristors: Materials Engineering and Neural Networks. *Adv. Funct. Mater.* **31**, 2006773 (2021).
6. Choi, S., Yang, J. & Wang, G. Emerging Memristive Artificial Synapses and Neurons for Energy-Efficient Neuromorphic Computing. *Adv. Mater.* **32**, 2004659 (2020).
7. Esqueda, I. S. et al. Aligned Carbon Nanotube Synaptic Transistors for Large-Scale Neuromorphic Computing. *ACS Nano.* **12**, 7352–7361 (2018).
8. Danial, L. et al. Two-terminal floating-gate transistors with a low-power memristive operation mode for analogue neuromorphic computing. *Nat. Electron.* **2**, 596–605 (2019).
9. Jiao, F. et al. Monatomic 2D phase-change memory for precise neuromorphic computing. *Appl. Mater. Today.* **20**, 100641 (2020).
10. Chua, L. Memristor-The Missing Circuit Element. *IEEE Trans. Circuit Theory* **18**, 507–519 (1971).
11. Strukov, D. B., Snider, G. S., Stewart, D. R. & Williams, R. S. The missing memristor found. *Nature* **453**, 80–83 (2008).
12. Yan, X. et al. Vacancy-Induced Synaptic Behavior in 2D WS_2 Nanosheet–Based Memristor for Low-Power Neuromorphic Computing. *Small* **15**, 1901423 (2019).
13. Ju, J. H. et al. Two-Dimensional MXene Synapse for Brain-Inspired Neuromorphic Computing. *Small* **17**, 2102595 (2021).
14. Vu, Q. A. et al. A High-On/Off-Ratio Floating-Gate Memristor Array on a Flexible Substrate via CVD-Grown Large-Area 2D Layer Stacking. *Adv. Mater.* **29**, 1703363 (2017).
15. Wang, K. et al. A Pure $2H-MoS_2$ Nanosheet-Based Memristor with Low Power Consumption and Linear Multilevel Storage for Artificial Synapse Emulator. *Adv. Electron. Mater.* **6**, 1901342 (2020).
16. Li, N. et al. Large-scale flexible and transparent electronics based on monolayer molybdenum disulfide field-effect transistors. *Nat. Electron.* **3**, 711–717 (2020).
17. Yi, J. et al. Double-Gate MoS_2 Field-Effect Transistors with Full-Range Tunable Threshold Voltage for Multifunctional Logic Circuits. *Adv. Mater.* **33**, 2101036 (2021).
18. Gant, P. et al. A strain tunable single-layer MoS_2 photodetector. *Mater. Today.* **27**, 8–13 (2019).
19. Lan, H. Y. et al. Gate-Tunable Plasmon-Enhanced Photodetection in a Monolayer MoS_2 Phototransistor with Ultrahigh Photoresponsivity. *Nano Lett.* **21**, 3083–3091 (2021).
20. Xu, R. et al. Vertical MoS_2 Double-Layer Memristor with Electrochemical Metallization as an Atomic-Scale Synapse with Switching Thresholds Approaching 100 mV. *Nano Lett.* **19**, 2411–2417 (2019).
21. Feng, X. et al. A Fully Printed Flexible MoS_2 Memristive Artificial Synapse with Femtojoule Switching Energy. *Adv. Electron. Mater.* **5**, 1900740 (2019).
22. Wang, M. et al. Robust memristors based on layered two-dimensional materials. *Nat. Electron.* **1**, 130–136 (2018).
23. Wang, X. et al. Grain-Boundary Engineering of Monolayer MoS_2 for Energy-Efficient Lateral Synaptic Devices. *Adv. Mater.* **33**, 2102435 (2021).
24. Sangwan, V. K. et al. Multi-terminal memtransistors from polycrystalline monolayer molybdenum disulfide. *Nature* **554**, 500–504 (2018).
25. Wang, L. et al. Artificial Synapses Based on Multiterminal Memtransistors for Neuromorphic Application. *Adv. Funct. Mater.* **29**, 1901106 (2019).
26. Krishnaprasad, A. et al. MoS_2 Synapses with Ultra-low Variability and Their Implementation in Boolean Logic. *ACS Nano.* **16**, 2866–2876 (2022).
27. Zou, J. et al. Doping Concentration Modulation in Vanadium-Doped Monolayer Molybdenum Disulfide for Synaptic Transistors. *ACS Nano.* **15**, 7340–7347 (2021).
28. Cho, S. et al. Phase patterning for ohmic homojunction contact in $MoTe_2$. *Science* **349**, 625–628 (2015).
29. Chuang, H. J. et al. Low-Resistance 2D/2D Ohmic Contacts: A Universal Approach to High-Performance WSe_2, MoS_2, and $MoSe_2$ Transistors. *Nano Lett.* **16**, 1896–1902 (2016).
30. Farmanbar, M. & Brocks, G. Controlling the Schottky barrier at MoS_2/metal contacts by inserting a BN monolayer. *Phys. Rev. B* **91**, 161304 (2015).
31. Liu, Y. et al. Toward barrier free contact to molybdenum disulfide using graphene electrodes. *Nano Lett.* **15**, 3030–3034 (2015).
32. Huh, W. et al. Synaptic Barristor Based on Phase-Engineered 2D Heterostructures. *Adv. Mater.* **30**, 1801447 (2018).
33. Li, Q. et al. Low voltage and robust InSe memristor using van der Waals electrodes integration. *Int. J. Extrem. Manuf.* **3**, 045103 (2021).
34. Choi, S. et al. Scalable Two-Dimensional Lateral Metal/Semiconductor Junction Fabricated with Selective Synthetic Integration of Transition-Metal-Carbide (Mo_2C)/-Dichalcogenide (MoS_2). *ACS Appl. Mater. Interfaces.* 11, 47190–47196 (2019).
35. Jeon, J. et al. Transition-Metal-Carbide (Mo_2C) Multiperiod Gratings for Realization of High-Sensitivity and Broad-Spectrum Photodetection. Adv. Funct. Mater. 29, 1905384 (2019)..
36. Yang, L. et al. Fabrication of MoO_x/Mo_2C-Layered Hybrid Structures by Direct Thermal Oxidation of Mo_2C. *ACS Appl. Mater. Interfaces.* **12**, 10755–10762 (2020).
37. Yang, L. et al. Resistance Switching and Failure Behavior of the MoO_x/Mo_2C Heterostructure. *ACS Appl. Mater. Interfaces.* **13**, 41857–41865 (2021).
38. Li, H. et al. From bulk to monolayer MoS_2: Evolution of Raman scattering. *Adv. Funct. Mater.* **22**, 1385–1390 (2012).
39. Faizan, M. et al. $MoS_2@Mo_2C$ hybrid nanostructures formation as an efficient anode material for lithium-ion batteries. *J. Mater. Res. Technol.* 14, 2382–2393 (2021).
40. Parthé, E. & Sadogopan, V. The structure of dimolybdenum carbide by neutron diffraction technique. *Acta Crystallogr.* **16**, 202–205 (1963).
41. Shi, Y. et al. Electronic synapses made of layered two-dimensional materials. *Nat. Electron.* **1**, 458–465 (2018).
42. Ge, R. et al. Atomristor: Nonvolatile Resistance Switching in Atomic Sheets of Transition Metal Dichalcogenides. *Nano Lett.* **18**, 434–441 (2018).
43. Wang, K., Chen, J. & Yan, X. MXene Ti_3C_2 memristor for neuromorphic behavior and decimal arithmetic operation applications. *Nano Energy.* **79**, 105453 (2021).
44. Le, D., Rawal, T. B. & Rahman, T. S. Single-layer MoS_2 with sulfur vacancies: Structure and catalytic application. *J. Phys. Chem. C.* **118**, 5346–5351 (2014).
45. Guzman, D. M., Onofrio, N. & Strachan, A. First principles investigation of copper and silver intercalated molybdenum disulfide. *J. Appl. Phys.* **121**, 055703 (2017).
46. Yin, L. et al. High-Performance Memristors Based on Ultrathin 2D Copper Chalcogenides. *Adv. Mater.* **34**, 2108313 (2022).
47. Chiu, F. C. A Review on Conduction Mechanisms in Dielectric Films. *Adv. Mater. Sci. Eng.* **2014**, 578168 (2014).
48. Chiu, F. C., Chou, H. W. & Lee, J. Y. M. Electrical conduction mechanisms of metal La_2O_3/Si structure. *J. Appl. Phys.* **97**, 103503 (2005).
49. Wang, C., He, W., Tong, Y. & Zhao, R. Investigation and Manipulation of Different Analog Behaviors of Memristor as Electronic Synapse for Neuromorphic Applications. *Sci. Rep.* **6**, 22970 (2016).
50. Yan, X. et al. Robust $Ag/ZrO_2/WS_2/Pt$ Memristor for Neuromorphic Computing. *ACS Appl. Mater. Interfaces* **11**, 48029–48038 (2019).
51. Bessonov, A. A. et al. Layered memristive and memcapacitive switches for printable electronics. *Nat. Mater.* **14**, 199–204 (2015).
52. Hus, S. M. et al. Observation of single-defect memristor in an MoS_2 atomic sheet. *Nat. Nanotechnol.* **16**, 58–62 (2021).
53. Gu, Y. et al. Sulfurization Engineering of One-Step Low-Temperature MoS_2 and WS_2 Thin Films for Memristor Device Applications. *Adv. Electron. Mater.* **8**, 2100515 (2022).
54. Lin, Y. et al. Transferable and Flexible Artificial Memristive Synapse Based on WO_x Schottky Junction on Arbitrary Substrates. *Adv. Electron. Mater.* **4**, 1800373 (2018).
55. Zucker, R. S. & Regehr, W. G. Short-term synaptic plasticity. *Annu. Rev. Physiol.* **64**, 355–405 (2002).
56. Ohno, T. et al. Short-term plasticity and long-term potentiation mimicked in single inorganic synapses. *Nat. Mater.* **10**, 591–595 (2011).
57. Wei, H. et al. Mimicking efferent nerves using a graphdiyne-based artificial synapse with multiple ion diffusion dynamics. *Nat. Commun.* **12**, 1068 (2021).

58. Zhang, S. et al. Selective Release of Different Neurotransmitters Emulated by a p–i–n Junction Synaptic Transistor for Environment-Responsive Action Control. *Adv. Mater.* **33**, 2007350 (2021).

59. Voglis, G. & Tavernarakis, N. The role of synaptic ion channels in synaptic plasticity. *EMBO Rep.* **7**, 1104–1110 (2006).

60. Lee, T. H. et al. Synaptic Plasticity and Metaplasticity of Biological Synapse Realized in a $KNbO_3$ Memristor for Application to Artificial Synapse. *ACS Appl. Mater. Interfaces* **10**, 25673–25682 (2018).

61. Ding, G. et al. Reconfigurable 2D WSe_2-Based Memtransistor for Mimicking Homosynaptic and Heterosynaptic Plasticity. *Small* **17**, 2103175 (2021).

62. Liu, L., Zhao, J., Cao, G., Zheng, S. & Yan, X. A Memristor-Based Silicon Carbide for Artificial Nociceptor and Neuromorphic Computing. *Adv. Mater. Technol.* **6**, 2100373 (2021).

63. Lan, J., Cao, G., Wang, J. & Yan, X. Artificial nociceptor based on TiO_2 nanosheet memristor. *Sci. China Mater.* **64**, 1703–1712 (2021).

64. Ilyas, N. et al. Analog Switching and Artificial Synaptic Behavior of Ag/SiOx:Ag/TiOx/p^{++}-Si Memristor Device. *Nano Res. Lett.* **15**, 30 (2020).

65. Pan, Y. et al. Mimicking synaptic plasticity and learning behaviours in solution processed SnO_2 memristor. *J. Alloy. Compd.* **757**, 496–503 (2018).

66. Zeng, S. Y., Zhou, Y. & Han, S. Phosphorene nano-heterostructure based memristors with broadband response synaptic plasticty. *J. Mater. Chem. C.* **6**, 9383–9393 (2018).

ACKNOWLEDGEMENTS

AUTHOR CONTRIBUTIONS

The preparation of Mo_2C, and Mo_2C/MoS_2 hybrid structure was completed by X.T., L.L.Y. and B.H.L.; the fabrication of devices completed by X.T., J.H.H. and B.H.L.; the characterization 2D materials were carried out by S.D.Y. and R.L.Y.; the test of memristors and artificial synapse were implemented by X.T., L.L.Y. and J.H.H.; the device structure design, and performance analysis were completed by W.J.C., Z.P.Z., Z.K.T. and X.C.G.; X.C.G. and X.T. contributed to the writing and polishing of the manuscript; X.C.G. supervised the overall research.

COMPETING INTERESTS

The authors declare no competing interests.

ADDITIONAL INFORMATION

Supplementary information The online version contains supplementary material available at https://doi.org/10.1038/s41528-022-00227-y.

Correspondence and requests for materials should be addressed to Xuchun Gui.

Reprints and permission information is available at http://www.nature.com/reprints

Publisher's note Springer Nature remains neutral with regard to jurisdictional claims in published maps and institutional affiliations.